International Journal of Thermal Sciences 226 (2026) 110880

Contents lists available at ScienceDirect

International Journal of Thermal Sciences

journal homepage: www.elsevier.com/locate/ijts

Atomic-scale insights into helium-induced thermal transport evolution in copper for plasma-facing components: A non-equilibrium molecular dynamics approach

Rui Jin [a,c], Hanlong Wang [a], Qing Peng [b], Hai Huang [a,*]

[a] Key Laboratory of Material Physics, Ministry of Education, School of Physics, Zhengzhou University, Zhengzhou, 450001, China
[b] School of Power and Mechanical Engineering, Wuhan University, Wuhan, 430072, China
[c] Physics Teaching and Research Group, Zhengzhou No.16 High School, Zhengzhou, 450007, China

ARTICLE INFO

Keywords:
Copper
Thermal transport
Helium
Clustering
Fusion reactor divertor
Non-equilibrium molecular dynamics

ABSTRACT

Copper alloys are critical heat-sink materials in fusion reactors but suffer severe thermal transport degradation under neutron irradiation, primarily due to helium generation. The atomistic mechanisms governing this degradation, however, remain insufficiently understood. This study employs non-equilibrium molecular dynamics simulations to systematically probe the thermal transport behavior of helium-containing copper by isolating the effects of three key variables: interstitial helium concentration, helium bubble pressure, and ambient temperature. Results reveal that dispersed helium reduces thermal conductivity by up to 47% at 8000 appm, driven by lattice strain and clustering, which strongly scatter phonons and suppress low-frequency modes. For systems containing a nanoscale bubble, Kapitza resistance becomes the dominant barrier, increasing sharply with bubble pressure. Remarkably, this interfacial resistance increases linearly with temperature—a trend that deviates from the behavior commonly observed at solid/solid interfaces. This anomalous trend is attributed to the compressible gas-like nature of the bubble interior. Elevated temperatures universally exacerbate degradation by thermally activating helium diffusion, bubble growth, and enhanced clustering, which collectively intensify phonon scattering. The findings establish a dual-mechanism framework for performance prediction and inform the design of irradiation-tolerant copper alloys for fusion applications.

1. Introduction

Fusion energy offers a promising route to a virtually limitless, safe, and carbon-free power source, establishing its potential as a cornerstone of future sustainable energy systems [1]. The feasibility of commercial fusion, however, is critically contingent upon the durability and reliable performance of its structural materials [2–4]. Within the intense environment of the reactor core, these materials are simultaneously subjected to extreme thermal loads and severe radiation damage from 14.1 MeV neutrons [5–7]. This high-flux neutron bombardment initiates significant degradation of the material's microstructure, primarily by creating point defects like vacancies and self-interstitial atoms [8–11]. These defects are highly mobile and subsequently coalesce to form a multitude of extended clusters, such as dislocation loops and voids [12–14]. Simultaneously, nuclear transmutation reactions introduce substantial concentrations of helium into the material lattice [9,15,16]. Because helium possesses negligible solubility in metals, it preferentially migrates to and is trapped by these irradiation-induced defects [17,18]. This sequestration of He atoms facilitates the nucleation of stabilized bubbles, which then grow larger under elevated operational temperatures [19]. The cumulative effect of these microscopic changes ultimately manifests as detrimental macroscopic properties—including hardening, embrittlement, volumetric swelling, and surface blistering—which compromise component integrity and precipitate premature failure [20–23].

Copper and its alloys are extensively utilized in fusion reactors owing to an exceptional blend of mechanical strength, thermal stability, and high thermal conductivity (TC) [3,24–27]. Their role is especially crucial in the divertor, a key reactor assembly, where Cu-based alloys stand out as the primary material choice for heat sinks [3,24,25]. This component, however, operates in the reactor's most severe environment; its plasma-facing surfaces must withstand a grueling combination of

* Corresponding author.
E-mail address: huanghai@zzu.edu.cn (H. Huang).

https://doi.org/10.1016/j.ijthermalsci.2026.110880
Received 26 January 2026; Received in revised form 27 February 2026; Accepted 24 March 2026
Available online 27 March 2026

intense heat fluxes (up to 20 MW•m^{-2}), heavy irradiation damage (above 14.0 dpa), and high concentrations of transmutation-generated helium (thousands of atomic parts per million (appm)) [2,3,28–30]. Extensive research has established that this exposure to neutron irradiation significantly impairs the TC of the copper heat sinks [26,31–34]. For example, atomistic simulations performed by Ye et al. [31] demonstrated that various point defects—most notably doping defects—impede the thermal transport carried by electrons in copper, thus diminishing the material's overall conductivity. Through *in-situ* transient grating spectroscopy experiments, Trachanas et al. [32] observed that proton irradiation induced a considerable decrease (10.86%) in copper's thermal diffusivity, while self-ion irradiation resulted in a markedly smaller reduction (~3%). They concluded that the specific defect configurations produced by each irradiating particle account for this difference, identifying implanted hydrogen as a likely factor in the pronounced degradation associated with protons. Further evidence from time-domain thermoreflectance experiments by Sun et al. [33] established a direct correlation between increasing He ion fluence and the severity of TC degradation. Based on such empirical evidence, Fabritsiev et al. [26] forecast that the synergistic impact of displacement damage and transmutation will cause a 17% total reduction in the TC of the CuCrZr alloy within ITER at an exposure of 5 dpa. The consequences of such degradation are severe, as diminished heat dissipation would elevate component temperatures and intensify thermal stresses, particularly at bimetallic joints like steel/copper or tungsten/copper [34]. This cascade of effects directly threatens to curtail the service lifetime of the divertor and first wall components. Despite these findings, the atomistic origins of thermal transport degradation in Cu-based materials under irradiation, particularly the influence of neutron-generated helium, remain inadequately characterized.

Over recent decades, molecular dynamics (MD) simulations have emerged as a prominent method for investigating the formation and development of irradiation-induced defects, helium clustering, and the thermal behavior of irradiated materials at picosecond–nanometer scales [10,35–37]. Notably, the non-equilibrium MD (NEMD) technique has established itself as a leading approach for modeling thermal conduction in nanoscale systems and has contributed significantly to elucidating thermal transport behavior in materials containing He atoms produced by nuclear transmutation [38–41]. For example, Petersson et al. [40] showed that low concentrations of helium in tungsten considerably diminish TC, although this reduction can be partially offset by vacancy-helium complexes that trap helium and alleviate crystal lattice strain. In contrast, Sharma et al. [41] reported that in nickel, larger helium bubble size and higher helium density increase both the local thermal gradient and interfacial Kapitza resistance near bubbles. Consequently, the demonstrated success of MD investigations across diverse material systems indicates that using NEMD technique to examine helium-induced evolution of thermal transport in copper is a feasible approach within practical simulation timeframes.

Therefore, in this work NEMD simulations are utilized to systematically probe the atomistic-scale thermal transport characteristics of copper in the presence of helium. Our analysis aims to disentangle the individual and interactive roles of three principal factors: the concentration of helium interstitials, the internal pressure of helium bubbles (expressed via the helium-to-vacancy (He/V) ratio), and the system temperature. Multiple metrics—including the spatial temperature distribution, TC, Kapitza interfacial resistance, and phonon density of states (PDOS)—are analyzed to uncover the underlying microstructural mechanisms responsible for thermal transport degradation. The paper is organized as follows: computational details are provided in Section 2; Section 3 examines the results related to helium concentration, bubble pressure, and temperature effects; and final conclusions are drawn in Section 4.

2. Simulation methodology

The copper-helium system was modeled using an embedded atom method (EAM) interatomic potential parameterized by Kashinath et al. [42], which explicitly accounts for interactions between Cu–Cu, Cu–He, and He–He atoms. A monocrystalline copper supercell containing 135, 000 atoms was initially constructed for the NEMD simulations, with dimensions of $15a_0 \times 15a_0 \times 150a_0$, where $a_0 = 3.615$ Å denotes the lattice constant. The crystal was aligned along the [110]||x, [$\bar{1}$10]||y, and [001]||z crystallographic orientations. Periodic boundary conditions were imposed along all three Cartesian axes to reproduce bulk-like material behavior. To simulate material states resulting from neutron transmutation or combined displacement damage and helium production, either a specific concentration of He atoms was randomly introduced into the supercell or a spherical void was generated at its center and filled with helium to mimic a bubble configuration [41,43]. The structure then underwent stress relaxation via conjugate gradient energy minimization at zero external pressure. Finally, the helium-containing system was thermally equilibrated for 20 ps in the NPT ensemble using a Nose–Hoover thermostat before proceeding with thermal transport analysis.

Thereafter, a thermal gradient was established by fixing the outermost layers (each 3.0 Å in thickness) at the simulation cell's extremities, which disrupted the periodic boundary conditions in the x-direction (see Fig. 1). Next to these immobilized regions, two 15.0 Å-thick reservoirs were positioned to apply a steady heat flux of 5.5×10^9 W m^{-2}. Thermal energy was added to the left-side reservoir (acting as the heat source), flowed directionally through the structure, and extracted from the right-side reservoir (serving as the heat sink). In the core adiabatic zone, atomic motions followed the microcanonical (NVE) ensemble, whereas the reservoir temperatures were regulated using Langevin thermostats. Once the system reached stability after an initial 0.2 ns relaxation phase, temperature measurements were gathered over another 4 ns timeframe to enable temporal averaging. Spatial temperature profiles were obtained by recording local temperatures within 12.7 Å-thick segments along the x-axis, allowing assessment of thermal transport performance in helium-containing copper. Three separate parameter studies were conducted: the first assessed the impact of interstitial helium concentration (0–8000 appm) in the absence of prior vacancies and under a 300 K thermostat; the second probed the influence of helium bubble pressure by adjusting the He/V ratio (0–3.0) in a 30.0 Å diameter bubble at 300 K; the third examined temperature effects ranging from 300 to 900 K on the preceding setups, keeping the interstitial helium concentration or He/V ratio fixed at 6000 appm or 2.5.

Note that all simulations employed the heat flux of 5.5×10^9 W m^{-2}. This intentionally elevated flux—higher than typical experimental conditions—was selected to improve the resolution of measurable temperature gradients, an approach consistent with established computational methodologies [44,45]. To account for stochastic variations in defect configurations, each simulation was repeated three times, and the results were averaged. Additional details regarding simulation parameters can be found in the prior publication [26,29,30,46]. Moreover, validation studies on defect-free copper crystals at 300 K in prior efforts [46], using Fourier's law ($J = -\kappa \bullet dT/dx$, where J represents heat flux, κ denotes TC, and dT/dx is the temperature gradient [47]) after 4 ns of thermal relaxation, has yielded a TC value of 7.98 W m^{-1} K^{-1}. This outcome shows close agreement with the literature value of 7.86 W m^{-1} K^{-1} [48], supporting the validity of our computational approach. All MD simulations were conducted using LAMMPS code [49], and atomic configurations were visualized and analyzed with OVITO software [50].

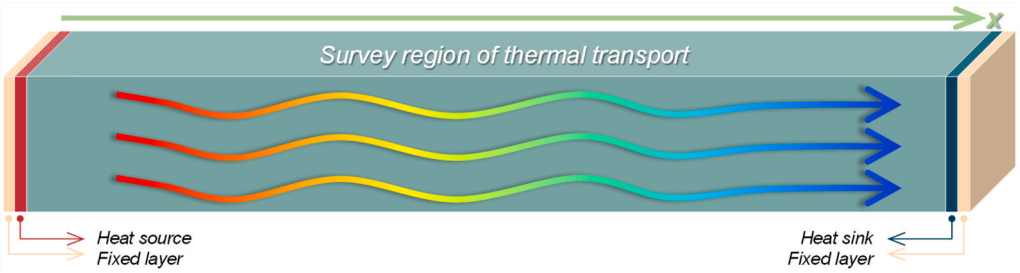

Fig. 1. Conceptual configuration of the computational domain employed in the NEMD simulation, depicting key components such as the heat source, heat sink, fixed boundary layers, and the central adiabatic region.

3. Results and discussion

3.1. Influence of helium concentration

The influence of interstitial helium concentration on thermal transport in copper was initially evaluated at 300 K. Fig. 2(a) displays the steady-state temperature profiles obtained after a 4 ns thermal relaxation period. All profiles exhibited excellent linearity along the simulation cell, confirming a linear response to the applied thermal gradient—a defining characteristic of the linear response regime. All configurations show a marked temperature elevation in the vicinity of the heat source and a concurrent drop near the heat sink. With increasing helium concentration, the temperature near the source rises steadily, whereas the sink-side profile shows minimal variation. Consequently, a more pronounced temperature gradient develops at higher helium levels, signifying greater phonon scattering and thermal

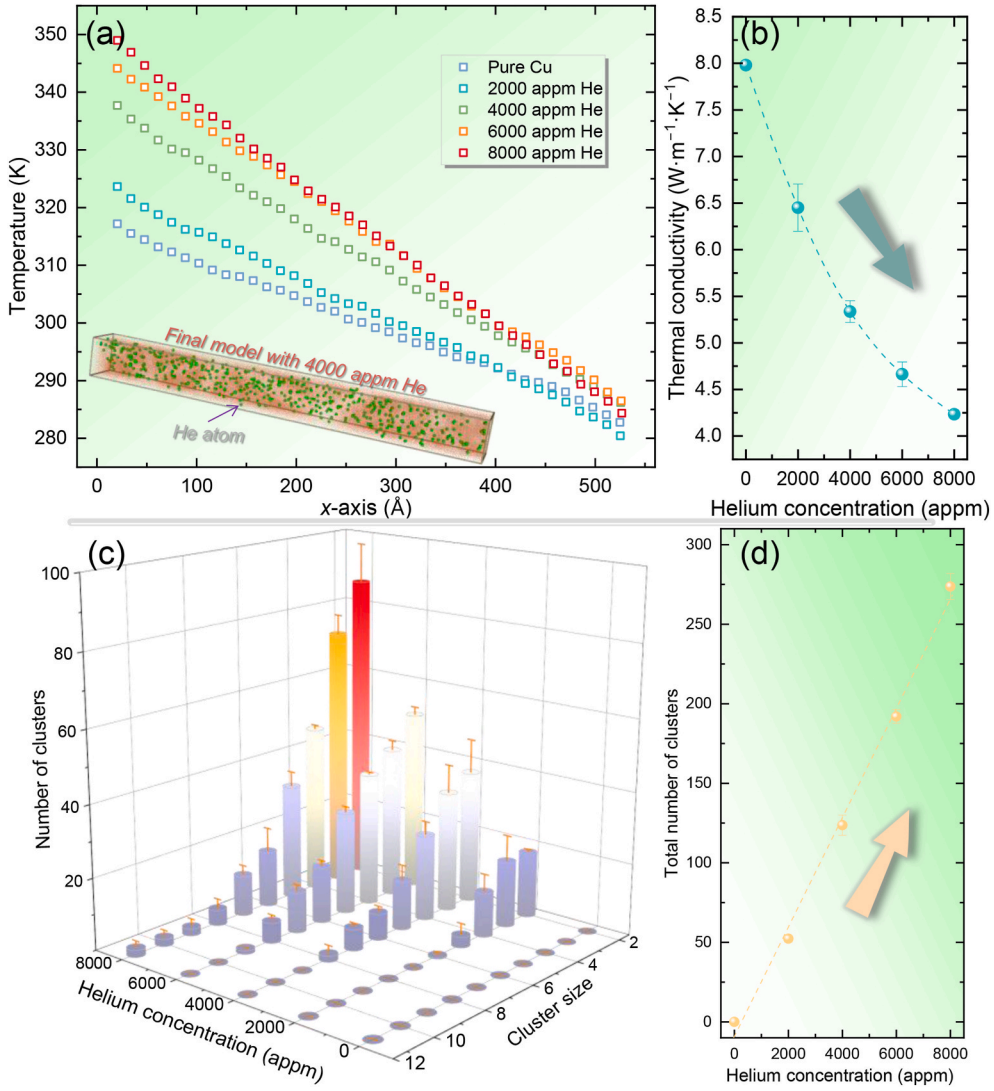

Fig. 2. Thermal properties and helium clustering behavior in copper systems with varying interstitial helium concentrations at 300 K, obtained after a 4-ns thermal relaxation period. (**a**) Steady-state temperature profiles along the simulation cell. (**b**) TC as a function of helium concentration. (**c**) Distribution of helium cluster sizes across different concentrations. (**d**) Total number of helium clusters versus helium concentration.

resistance in the material. This gradient, derived from linear fits to the data in Fig. 2(a), was applied within Fourier's law to compute TC, with the results plotted in Fig. 2(b). A consistent, concentration-dependent reduction in TC is observed. Notably, a helium concentration of 8000 appm leads to a decrease of approximately 47% relative to pristine copper. This suppression stems from helium-induced lattice strain, which shortens the phonon mean free path—a mechanism consistent with Klemens' theory [51]. The decline is particularly steep at concentrations below 4000 appm. Rahman et al. [52] reported analogous behavior in carbon-doped silylene, attributing it to isolated impurity atoms acting as efficient, independent scattering centers at low doping levels—an interpretation that likely applies here, where dispersed He atoms profoundly disrupt phonon propagation and cause an accelerated initial decrease in conductivity. To test this interpretation, cluster analysis was performed on He atoms within systems of different concentrations, employing a cutoff radius of 2.48 Å [53]; the results are presented in Fig. 2(c). The data show a clear rise in both the population of helium clusters and the propensity for larger cluster formation at elevated helium concentrations. As an example, the maximum cluster size identified is 6 atoms at 2000 appm, compared to clusters containing up to 12 atoms at concentrations above 6000 appm. The presence of these larger aggregates results in more significant lattice strain, thereby intensifying phonon scattering and shortening the mean free path [54]. The quantitative relationship between helium concentration and the total count of clusters is further illustrated in Fig. 2(d), which demonstrates a nearly linear correlation. This increase in cluster density provides additional sites for phonon scattering. Consequently, the degradation of TC with rising helium concentration arises from a dual effect: the growth in average cluster size and the concurrent increase in cluster population, which act in tandem to impede heat transfer. It is acknowledged that defect configurations inevitably evolve during thermal transport, particularly for temperature-sensitive helium-related defects. For example, in systems initially containing randomly dispersed interstitial He atoms, clustering emerges over the course of the simulation. However, this evolution reflects the intrinsic temperature-driven microstructural changes under investigation, rather than artifacts introduced by the heat flux itself. Critically, the analysis focuses on defect statistics and thermal transport properties after a fixed relaxation period of 4 ns, with all reported results averaged over multiple independent simulations to ensure statistical reliability.

Typically, PDOS analysis offers an indirect but valuable perspective on thermal transport mechanisms by quantifying changes in the vibrational spectrum [51,52]. The PDOS is calculated from MD trajectories by applying a fast Fourier transform to the atomic velocity autocorrelation function (VACF), as defined as follows [51,55].

$$\mathrm{PDOS}(\omega) = \int_{-\infty}^{\infty} e^{-i\omega t}\mathrm{VACF}(t)dt, \tag{1}$$

where

$$\mathrm{VACF}(t) = \frac{1}{N}\sum_{j=1}^{N}\langle v_j(0)v_j(t)\rangle. \tag{2}$$

Here, ω is the phonon frequency, N is the number of atoms in the sampled region, $v_j(t)$ is the velocity vector of the j_{th} atom at time t, and ⟨⋯⟩ denotes the ensemble average. Fig. 3(a–d) presents the computed PDOS for copper systems with helium concentrations ranging from 2000 to 8000 appm at 300 K, alongside the PDOS of a defect-free copper for reference. The spectra for all helium-containing systems are dominated by low-frequency phonon modes, primarily distributed between 0 and 10 THz, and exhibit a characteristic bimodal shape with a dominant peak at 4.6 THz and a secondary peak at 7.0 THz. This profile aligns with prior reports [46,55,56], corroborating the reliability of the present simulations. Relative to pristine copper, the PDOS peak intensities in helium-containing systems show a slight attenuation that becomes more pronounced with increasing helium concentration. For example, at 8000 appm, the integrated intensity of the primary peak (4.6 THz) decreases from 0.2323 to 0.2245, and that of the secondary peak (7.0 THz) declines from 0.2319 to 0.2242. This suppression likely stems from the localization of phonon modes due to lattice distortion around helium clusters and associated crystal defects, which restricts phonon propagation, confines vibrational energy, and thereby reduces TC [57]. On the other hand, to quantify phonon mode modifications in copper resulting from helium incorporation, the PDOS overlap factor (S) between helium-doped and defect-free systems was defined by the expression [55,56].

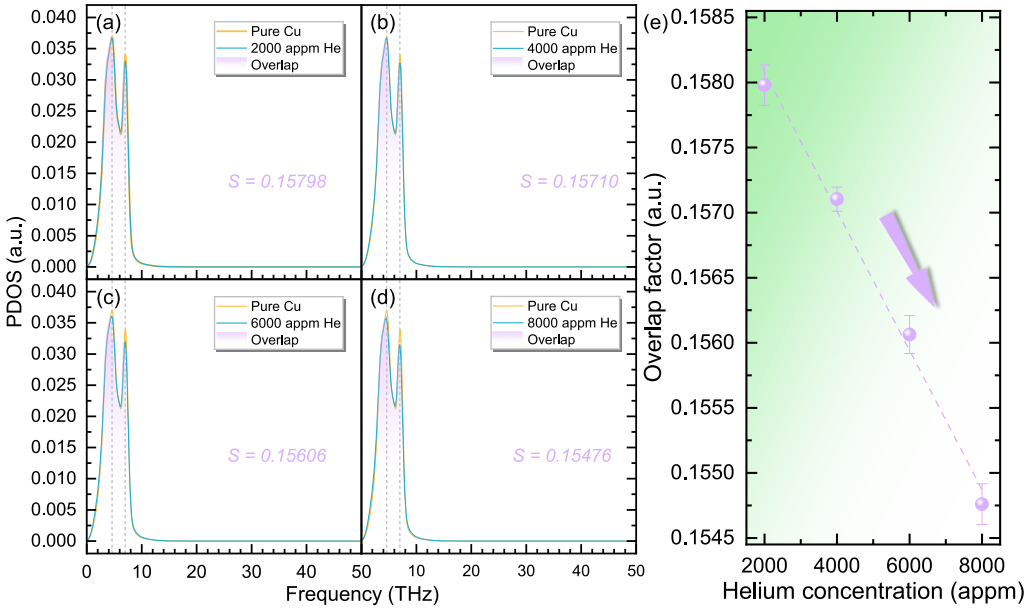

Fig. 3. Phonon-level analysis of thermal transport degradation in copper with varying helium concentrations at 300 K. (**a**–**d**) Calculated PDOS spectra for systems containing 2000 to 8000 appm helium, compared with the PDOS of defect-free copper. (**e**) PDOS overlap factor, quantifying the spectral deviation from pristine copper, plotted as a function of helium concentration to correlate with the observed reduction in TC.

$$S = \int_{-\infty}^{\infty} \min\{P_0(\omega), P_\mu(\omega)\} d\omega, \quad (3)$$

where $P_0(\omega)$ and $P_\mu(\omega)$ represent the PDOS of defect-free and helium-doped copper, respectively. Overlap occurs predominantly within the 0–10.0 THz frequency range. This factor, extracted from Fig. 3(a–d) and plotted as a function of helium concentration in Fig. 3(e), serves as a quantitative measure of the corresponding TC trend. The plot reveals a consistent decline in the overlap factor with increasing helium concentration. The overlap factor quantifies the degree of similarity between the vibrational spectrum of a helium-containing system and that of pristine copper. Physically, it reflects how significantly helium-induced defects alter the intrinsic phonon modes of the copper lattice. A decrease in this factor indicates a progressive PDOS modification induced by helium defects. Specifically, the introduction of helium interstitials and clusters distorts the copper lattice, breaking its translational periodicity and altering the vibrational modes. This lattice distortion enhances phonon scattering by disrupting the coherent propagation of lattice waves, particularly affecting low-frequency acoustic phonons that are the primary heat carriers. Since TC is directly proportional to the phonon relaxation time and group velocity, the observed spectral deviation—reflected in the declining overlap factor—provides a direct microscopic signature of the enhanced scattering processes responsible for the macroscopic reduction in TC. Thus, the consistent correlation between the overlap factor and TC across increasing helium concentrations confirms that phonon-level modifications are the fundamental origin of the thermal transport degradation.

3.2. Influence of helium-to-vacancy ratio

The transmutation of elements during neutron irradiation generates considerable amounts of helium within metallic crystals. Given helium's minimal solubility, these atoms readily agglomerate into nanoscale bubbles, a key microstructural feature in irradiated nuclear materials [6,22,35]. Consequently, assessing how such bubbles affect thermal transport in copper and its alloys is crucial. To investigate the underlying mechanisms, we examined the thermal transport in copper containing a 30.0 Å diameter helium bubble, with He/V ratios varying from 0 to 3.0 at 300 K. Fig. 4(a) presents the resulting steady-state temperature distributions following 4 ns of thermal relaxation. Unlike systems with randomly distributed helium interstitials, the temperature profile here is discontinuous, marked by a noticeable temperature drop near the bubble interface where the gradient sharpens relative to the bulk copper matrix. For example, a linear fit extrapolated to the interface in the He/V = 3.0 system indicates a temperature jump of roughly 10.7 K. This discontinuity becomes increasingly evident at higher He/V ratios, primarily attributable to the significant disparity in TC between copper and the helium bubble [46,55]. Elevated helium pressure within the bubble further suppresses the local TC, exacerbating the mismatch and hindering heat transfer. Such interfacial thermal barriers are conventionally expressed in terms of Kapitza resistance (R), defined as the inverse of interfacial thermal conductance (G) [55,56].

$$R = \frac{1}{G} = \frac{\Delta T}{J}, \quad (4)$$

where ΔT is the temperature drop across the bubble region, as annotated in Fig. 4(a). The calculated Kapitza resistances, derived from the ΔT values in Fig. 4(a), are plotted against He/V ratio in Fig. 4(b). A clear positive correlation emerges: the resistance rises from a baseline of 0.87 GW^{-1} m^2 K at He/V = 0 to 0.95 GW^{-1} m^2 K at He/V = 1.5, before accelerating sharply to 2.25 GW^{-1} m^2 K at He/V = 3.0—an increase by a factor of approximately 2.5 across the range studied.

As seen in Fig. 4(a), a higher He/V ratio correlates with an elevation in temperature on the copper's heat-source side and a concurrent reduction on the heat-sink side. Notably, however, the temperature gradients in both regions stay essentially constant and are scarcely influenced by the varying He/V ratio; these gradients also remain closely aligned across all conditions examined. Since the copper on either side of the bubble was initially helium-free and symmetrically arranged, and in light of the results discussed in subsection 3.1, it appears that He atoms did not migrate appreciably from the bubble into the surrounding copper matrix during thermal transport. Hence, in contrast to systems containing dispersed interstitial helium (Fig. 2), the copper bulk did not develop a distribution of helium clusters that could serve as variable phonon-scattering centers and modify the local temperature gradients. To examine this hypothesis further, radial distribution functions of both He and Cu atoms relative to the bubble center were computed. These distributions are shown in Fig. 5(a–d), where accompanying insets depict the local defect morphology near each bubble. A consistent single-peak profile emerges in the helium content distribution across every system examined. Within the bubble core, the helium fraction rises

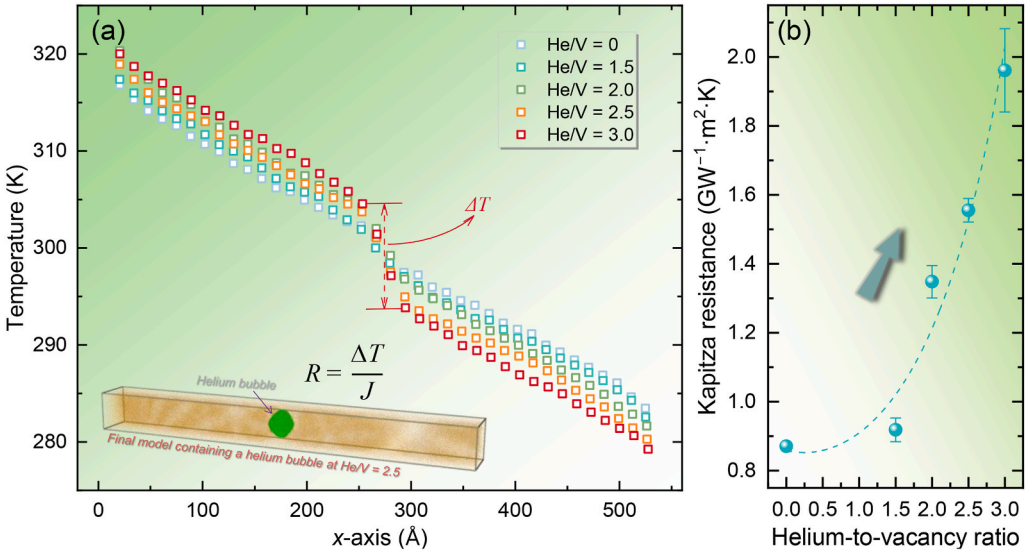

Fig. 4. Thermal transport characteristics in copper containing a 30 Å helium bubble across a range of He/V ratios (0–3.0) at 300 K after 4 ns of thermal relaxation. (**a**) Steady-state temperature profiles along the simulation cell. (**b**) Evolution of Kapitza resistance with He/V ratio, derived from the interfacial temperature discontinuity.

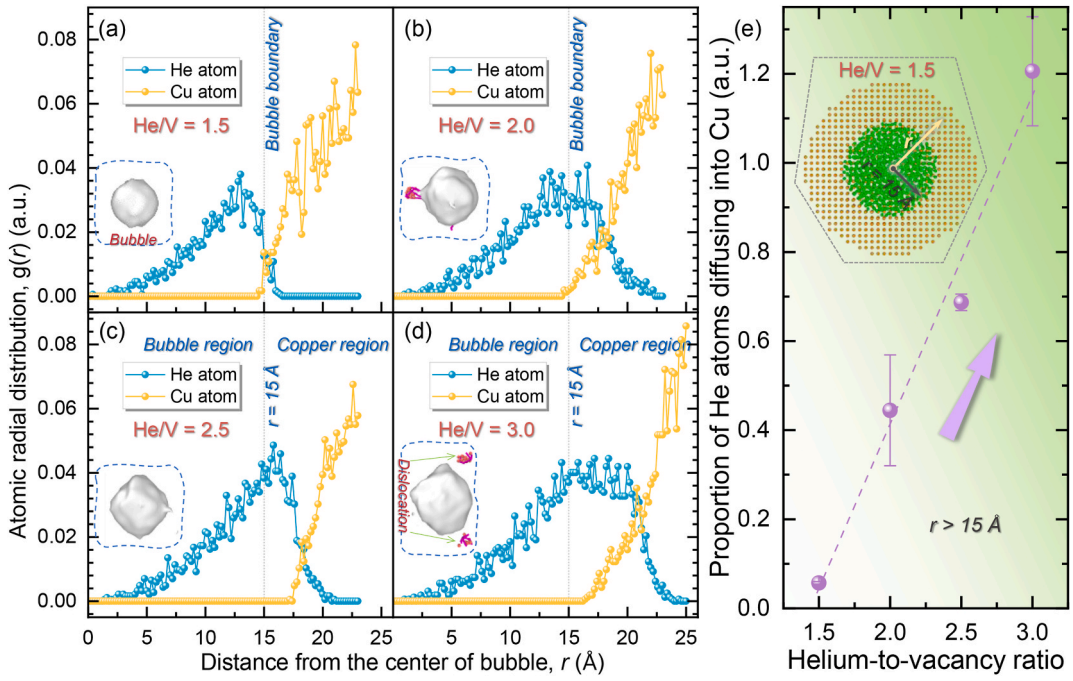

Fig. 5. Microstructural evolution near the Cu/bubble interface across different He/V ratios (1.5–3.0) at 300 K. (**a–d**) Radial distribution functions of He and Cu atoms relative to the bubble center. Corresponding defect configurations near the bubble are shown in the insets. (**e**) Fraction of He atoms diffusing beyond the initial bubble radius (r > 15.0 Å) versus He/V ratio.

almost linearly with radial distance r. Because the volume of each concentric shell increases with r, this linear dependence suggests a nearly uniform helium density throughout the core. As the He/V ratio grows, the spatial spread of the helium distribution widens, signaling bubble expansion and the gradual release of He atoms from the bubble into the adjacent copper lattice [43]. For a He/V ratio of 1.5, a reduction in the helium fraction is observed at the bubble periphery (near r = 15.0 Å), signifying an under-pressured bubble state. Under this condition, limited helium diffusion into the surrounding copper occurs, and the copper lattice exhibits negligible distortion, as visible in the inset of Fig. 5(a). The consequent minimal interfacial disturbance accounts for the only marginal increase in Kapitza resistance relative to a void. At He/V = 2.0, the helium fraction at the periphery attains a maximum. Compared to the 1.5 case, a greater number of He atoms diffuse into the copper matrix, extending to radial distances up to 22.5 Å. While the Cu atom distribution remains largely intact, the inset in Fig. 5(b) confirms that the bubble now induces noticeable lattice distortion and dislocation formation in the adjacent copper—behavior consistent with prior reports on helium-bubble evolution [58] and indicative of a pressure-release mechanism. This suggests a transition to a slightly over-pressured bubble state. The more substantial rise in Kapitza resistance for He/V = 2.0 can thus be linked to the increased population of He atoms on the copper side of the interface. These atoms serve dual roles: as direct phonon-scattering centers and as sources of lattice strain that further intensify phonon scattering, collectively degrading thermal conductance [59,60]. When the He/V ratio reaches 2.5, the maximum of helium fraction appears beyond the original bubble boundary (>15.0 Å), and the radial interval between 15.0 and 17.5 Å becomes entirely devoid of Cu atoms. These features point to bubble expansion driven by overpressure, which pushes Cu atoms out of their lattice sites. Notably, helium migration into the bulk copper at this ratio is more restrained than at He/V = 2.0. The absence of dislocations in the inset of Fig. 5(c) implies that pressure relief occurs predominantly via outward helium diffusion rather than through the nucleation of dislocations [58,61–63]. Accordingly, the additional rise in Kapitza resistance from He/V = 2.0 to 2.5 stems largely from the enlarged bubble size, which attenuates phonon transmission. At a He/V ratio of 3.0, the radial distribution profile of helium exhibits noticeable peak broadening compared to the system with He/V = 2.5, reflecting further intrusion of the bubble into the copper lattice. This outward expansion enlarges the bubble while simultaneously generating dislocations through lattice distortion in the neighboring copper, as depicted in the inset of Fig. 5(d). Strong overpressure also propels helium deeper into the copper, with atoms migrating as far as r ≈ 25.0 Å. Together, these mechanisms amplify phonon scattering, obstruct thermal transport, and produce a marked jump in Kapitza resistance. To quantify helium migration, Fig. 5 (e) plots the fraction of He atoms situated beyond r = 15.0 Å relative to the total helium content. This fraction grows nearly linearly with He/V ratio, correlating closely with the Kapitza resistance trend in Fig. 4(b) and confirming that interfacial thermal resistance increases with outward helium diffusion. Finally, helium penetration from the bubble into the copper matrix does not exceed 10 Å, confirming that the thermal influence of the bubble is localized to its immediate surroundings and does not significantly perturb the temperature gradient in distal copper regions.

To elucidate the underlying mechanisms of the observed thermal behavior, the PDOS was computed for copper systems containing a 30.0 Å helium bubble with He/V ratios from 0 to 3.0 at 300 K; the results are presented in Fig. 6(a–e), alongside the PDOS of a defect-free copper for reference. The characteristic bimodal distribution—consisting of a dominant peak at 4.6 THz and a secondary peak at 7.0 THz—persists and appears largely unaltered by the presence of the bubble. Relative to pristine copper, however, the PDOS peak intensities in helium-containing systems exhibit a slight attenuation that grows with increasing He/V ratio. For He/V ratios ≤1.5, the PDOS spectra show only minor deviations from that of pristine copper. This minimal variation accounts for the fact that the effective TC estimated via Maxwell's effective medium model remains comparable to that of a defect-free crystal [46], while the associated Kapitza resistance stays relatively small. In contrast, for He/V > 1.5, a noticeable suppression of the low-frequency PDOS peak emerges, accompanied by a relative enhancement of the high-frequency component. Low-frequency phonons correspond primarily to long-wavelength acoustic modes; their attenuation likely results from the outward diffusion of He atoms, which

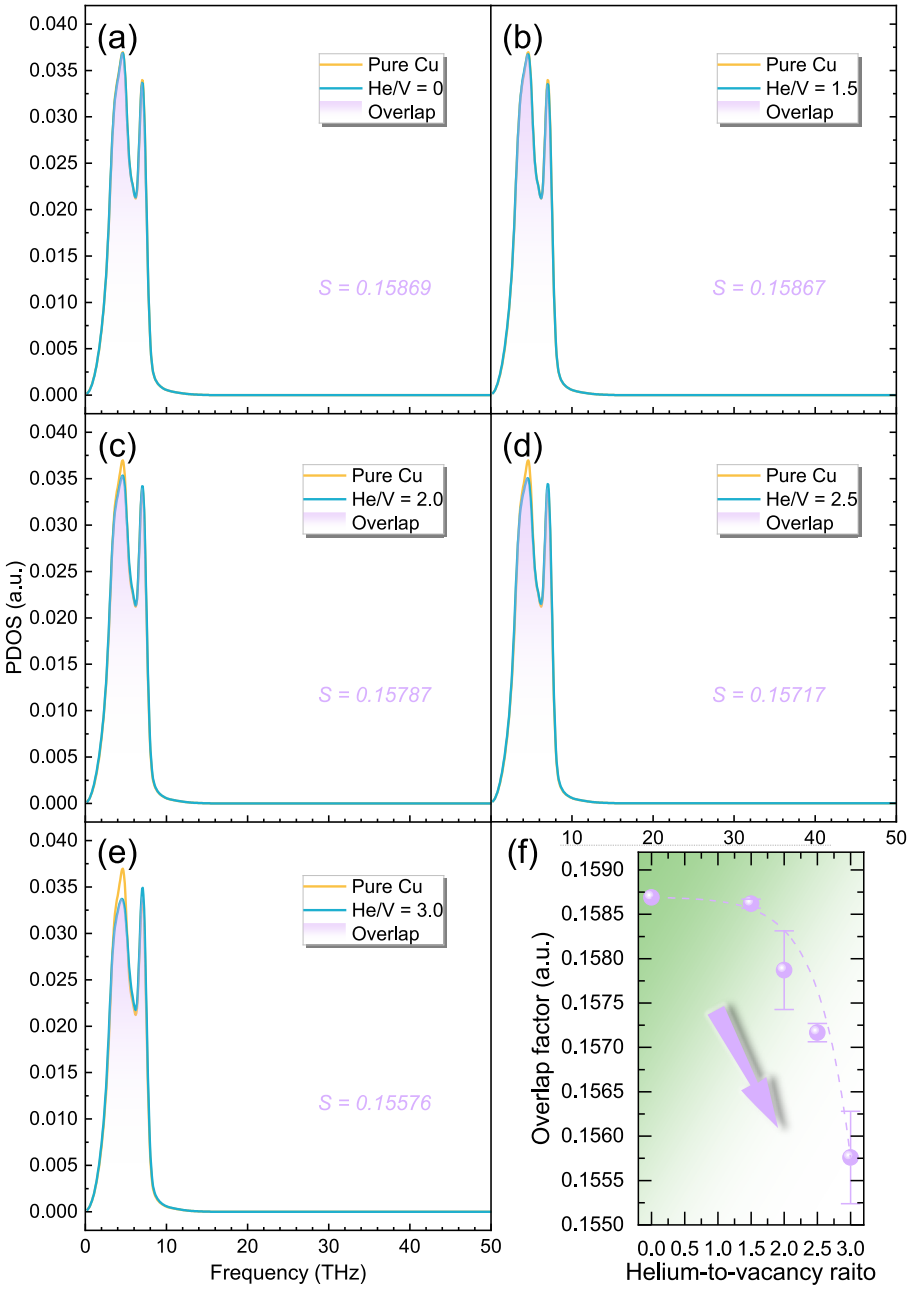

Fig. 6. Phonon-level analysis of thermal transport degradation in copper containing a 30 Å helium bubble at 300 K across different He/V ratios. (**a–e**) Calculated PDOS spectra for systems with He/V ratios ranging from 0 to 3.0, compared with the PDOS of defect-free copper. (**f**) PDOS overlap factor, quantifying the spectral deviation from pristine copper, plotted as a function of He/V ratio to correlate with the interfacial thermal resistance.

disrupts the local lattice periodicity and enlarges the bubble volume, thereby confining these phonon modes near the interface. Since low-frequency phonons contribute significantly to heat conduction [64], their confinement reduces the overall thermal transport capacity of the system, accounting for the concurrent rise in Kapitza resistance at higher He/V ratios. On the other hand, the observed enhancement of high-frequency peaks arises from the mass difference between He and Cu atoms. The lighter helium impurities introduce additional localized vibrational modes at higher frequencies, thereby increasing the phonon density in this spectral region [52]. Furthermore, the PDOS overlap factor, extracted from Fig. 6(a–e), is plotted against the He/V ratio in Fig. 6(f) to provide a quantitative link to the Kapitza resistance. This factor exhibits a gradual decline with increasing He/V ratio, a trend that correlates well with the corresponding decrease in interfacial thermal conductance shown in Fig. 4(b). The consistent behavior of both metrics confirms that a phonon-based interpretation effectively captures the influence of helium bubbles on thermal transport in copper.

3.3. Role of thermal environment

Temperature dependence is a fundamental characteristic of nanoscale thermal transport [52,54,55]. At elevated temperatures, enhanced thermal fluctuations and increased phonon anharmonicity typically lead to a reduction in TC. In perfect single crystals such as copper and graphene, this often follows an inverse relationship with temperature, known as the 1/T rule [54,65]. In contrast, some binary atomic structures display a more gradual decline in TC with rising temperature, a behavior primarily attributed to the dominant role of high-frequency optical phonons [54,66]. Moreover, research by Fang et al. [67] indicates that temperature variations can alter the diffusion behavior of

He atoms as well as the formation of helium bubbles and clusters. Given that structural materials in fusion reactor divertors operate under high temperatures and are subjected to intense heat fluxes, it is crucial to investigate how temperature influences thermal transport in helium-containing copper systems and to uncover the underlying mechanisms governing this dependence.

3.3.1. *Effect of temperature on systems with interstitial helium*

Building on earlier observations, the rate of TC reduction begins to decelerate in the copper system containing 6000 appm interstitial helium at 300 K, a point at which larger helium clusters form. These findings imply that the evolution of defect structures plays a more dominant role in governing thermal transport as helium concentration increases—an influence that is expected to become even more pronounced at elevated temperatures. To investigate this temperature dependence in detail, the copper system containing 6000 appm helium was served as the model for examining thermal transport behavior over the range of 300 to 900 K. Fig. 7(a) presents the resulting TC as a function of temperature, revealing a progressive decrease consistent with phonon-mediated conduction in nanoscale materials. Relative to the value at 300 K, conductivity declines by 28.46% at 500 K, 47.81% at 700 K, and 59.69% at 900 K, with the reduction rate gradually slowing. This behavior can be primarily explained by two interconnected mechanisms. First, at elevated temperatures the average phonon population rises approximately in proportion to temperature, as expressed by the following relation [68].

$$\bar{n}(q) = \frac{1}{e^{\hbar\omega_q / k_b T} - 1}, \tag{5}$$

where $\hbar$ is the reduced Planck constant, k_b the Boltzmann constant, and ω_q the vibrational frequency of mode q. This growth in phonon density elevates the probability of phonon-phonon scattering, shortening the mean free path and thereby lowering TC. Second, statistical analysis of helium clusters across temperatures (see Fig. 7(b)) reveals that cluster size generally expands with increasing temperature. While clusters of up to 10 He atoms appear at all temperatures above 300 K, aggregates containing 12 atoms emerge at 900 K. Furthermore, the total number of clusters exhibits an upward trend with temperature, and at 900 K nearly all He atoms (96.7%) participate in cluster formation. These findings, consistent with prior studies [67], indicate that higher temperatures promote helium clustering in copper. Because larger clusters introduce more severe lattice distortion than isolated interstitials, they intensify defect-phonon scattering. The combined action of these two temperature-driven effects—increased phonon density and enhanced helium clustering—thus accounts for the observed reduction in TC. Furthermore, although TC is traditionally derived from Fourier's law, a slight deviation from the standard 1/T dependence is observed at higher temperatures (Fig. 7(a)). Quantifying this divergence yields a scaling of approximately $1/T^{0.838}$, indicating that the rate of TC reduction with temperature is attenuated relative to that in perfect crystals. A similar trend has been reported in binary systems such as Si/Ge superlattices and GaN crystals [66,69]. This behavior parallels the concentration-dependent effect shown in Fig. 2(b), where increased helium clustering moderates the decline in conductivity. The underlying mechanism likely involves the enhancement of phonon–phonon Umklapp scattering or inelastic scattering by helium clusters at elevated temperatures [70]. An increased contribution from high-frequency phonons with rising temperature may further contribute to this moderated reduction rate [66].

To elucidate the underlying mechanisms of the anomalous TC trend, the temperature-dependent PDOS was computed, as shown in Fig. 8(a). With increasing temperature, the PDOS peaks exhibit broadening and a gradual suppression in intensity, consistent with the overall decline in TC. This behavior can be attributed to two primary, interconnected effects. First, rising temperature intensifies phonon-phonon anharmonic scattering, particularly three-phonon Umklapp processes, which degrade TC by impeding phonon momentum and shortening the phonon mean free path [71,72]. Second, elevated temperatures promote the growth and proliferation of helium clusters (as established in Fig. 7(b)), which induce more severe lattice distortion. This distortion enhances defect-phonon scattering and further reduces the group velocity and mean free path of phonons, effectively localizing a portion of the vibrational modes, especially at higher frequencies [52]. Notably, however, the rate of TC decrease moderates at higher temperatures (Fig. 7(a)). This deceleration is linked to an evolving spectral contribution: while low-frequency phonons dominate transport at lower temperatures, their role diminishes as temperature rises [54,66]. Concurrently, the PDOS inset in Fig. 8(a) reveals a relative enhancement in the high-frequency region (>10 THz). This shift signifies an increased population and participation of high-frequency phonons at elevated

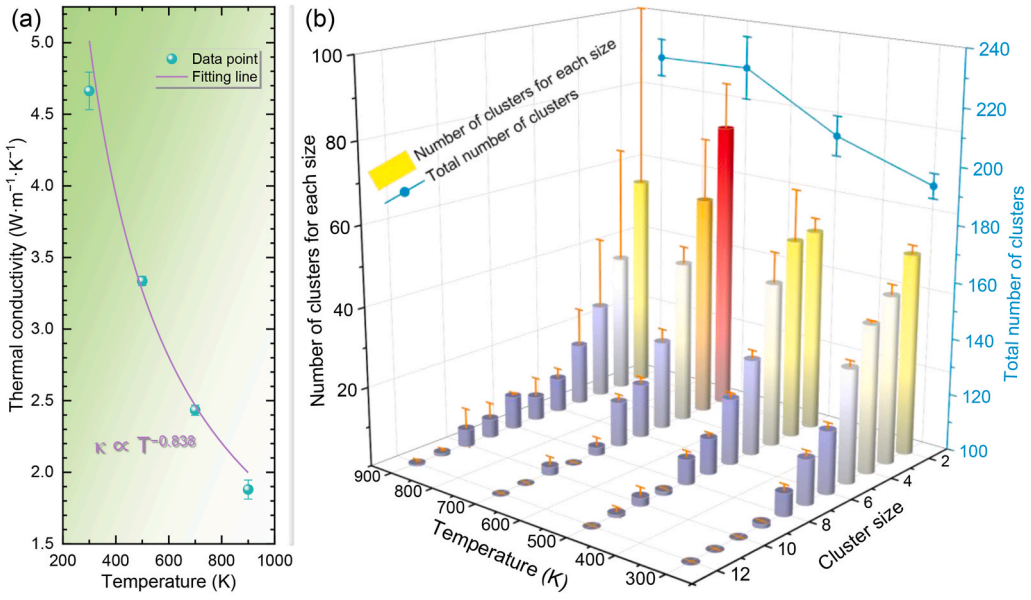

Fig. 7. Thermal properties and helium clustering behavior in copper containing 6000 appm interstitial helium across temperatures from 300 to 900 K, obtained after a 4-ns thermal relaxation period. (**a**) TC as a function of temperature. (**b**) Helium cluster size distributions and total cluster counts at different temperatures.

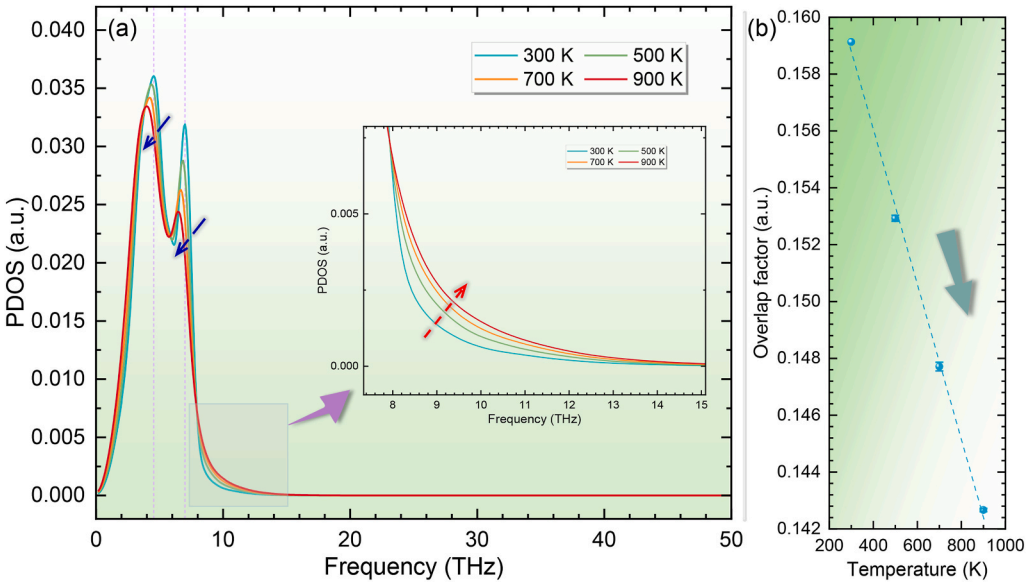

Fig. 8. Phonon-level analysis of the temperature-dependent thermal transport degradation in copper containing 6000 appm interstitial helium. (**a**) Calculated PDOS spectra for the system across temperatures (300–900 K). (**b**) PDOS overlap factor, quantifying the spectral deviation relative to the 300 K reference, plotted as a function of temperature; its decreasing trend quantifies the thermally induced alteration of phonon modes.

temperatures, a phenomenon partly enabled by the lighter mass of helium impurities which can introduce localized high-frequency modes [52]. Although these high-frequency carriers are inherently more susceptible to scattering and localization, their increased activity alters the dominant scattering regime [55,66]. At high temperatures, the contribution from temperature-sensitive Umklapp scattering (and potentially higher-order processes like four-phonon scattering) becomes increasingly significant [52]. In contrast, scattering from relatively static microstructural features, such as interfaces and helium clusters, exhibits a weaker temperature dependence [73,74]. The competition between these mechanisms—increasing high-frequency phonon activity versus temperature-activated anharmonic scattering—results in the attenuated scaling of TC with temperature (approaching $\sim 1/T^{0.838}$). This interpretation is further supported by the approximately linear decrease in the PDOS overlap factor with temperature shown in Fig. 8(b), which quantitatively correlates the changing phonon spectrum with the microstructural evolution (*e.g.*, helium clustering) discussed earlier.

3.3.2. *Effect of temperature on systems containing a helium bubble*

As established in previous sections, helium bubbles with He/V $\geq$ 2.5 at 300 K are overpressurized, leading to expansion into the copper matrix and a concomitant acceleration in the rate of interfacial thermal conductance degradation. Since elevated temperature enhances atomic diffusion, it is expected to intensify this effect. To investigate this temperature dependence, the system with He/V = 2.5 was studied across a range from 300 K to 900 K. Fig. 9(a) presents the steady-state temperature profiles around the bubble after 4 ns of thermal relaxation at different temperatures; the vertical axis scale is consistent across all profiles to facilitate direct comparison of temperature increments. The data reveal two key trends: first, the local temperature gradient near

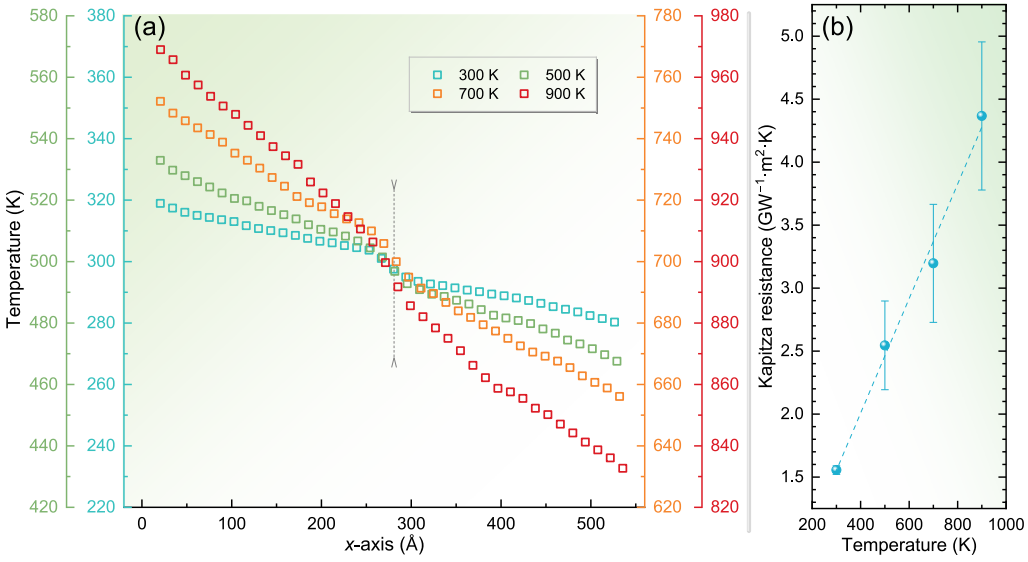

Fig. 9. Temperature-dependent thermal transport in copper containing a helium bubble at He/V = 2.5, examined from 300 to 900 K after 4 ns of thermal relaxation. (**a**) Steady-state temperature profiles along the simulation axis. (**b**) Evolution of Kapitza resistance with simulation temperature, calculated from the interfacial temperature jump.

the helium bubble steepens with increasing temperature; second, the overall temperature gradient within the bulk copper (non-bubble region) also increases significantly. This indicates a progressive inhibition of heat flow through the crystal at higher temperatures. The mechanism is twofold: rising temperature promotes the outward diffusion of helium from the bubble into the copper matrix, further expanding the bubble volume. Simultaneously, it increases the kinetic energy of He atoms within the bubble, raising its internal pressure [75,76]. As demonstrated in Section 3.2, higher bubble pressure widens the TC mismatch at the Cu/bubble interface, thereby impeding heat transfer. Furthermore, analysis of the temperature distributions shows that at T $\leq$ 700 K, the profile in the non-bubble region remains more linear than that in the bubble-affected zone, with a marked gradient difference between the two. At 900 K, however, the linearity in the non-bubble region decreases slightly, and the gradient difference becomes less pronounced. To quantitatively assess the temperature effect, the Kapitza resistance was calculated and plotted against temperature in Fig. 9(b). It exhibits a positive, approximately linear correlation, increasing from 1.56 to 4.37 GW^{-1} m^2 K over the temperature range studied, which confirms a declining thermal transport efficiency near the interface. Notably, this trend—increasing interfacial resistance with temperature—contrasts with the behavior typically observed at solid/solid interfaces [55,77], where resistance often decreases. This reversal is likely a distinctive feature of the solid/gas-like interface presented by the helium bubble, highlighting the unique phonon scattering dynamics dominated by the compressible gaseous interior under varying thermal conditions.

To verify that rising temperature exacerbates helium-bubble expansion and thereby impacts thermal transport, radial distribution functions for He and Cu atoms relative to the bubble center were calculated at various temperatures (see Fig. 10(a)). The profiles show that the spatial extent of helium broadens with increasing temperature, indicating progressive bubble growth and greater release of helium into the copper matrix. This outward expansion is accompanied by a widening region devoid of Cu atoms (*e.g.*, from 15.0 to 21.0 Å at 900 K),

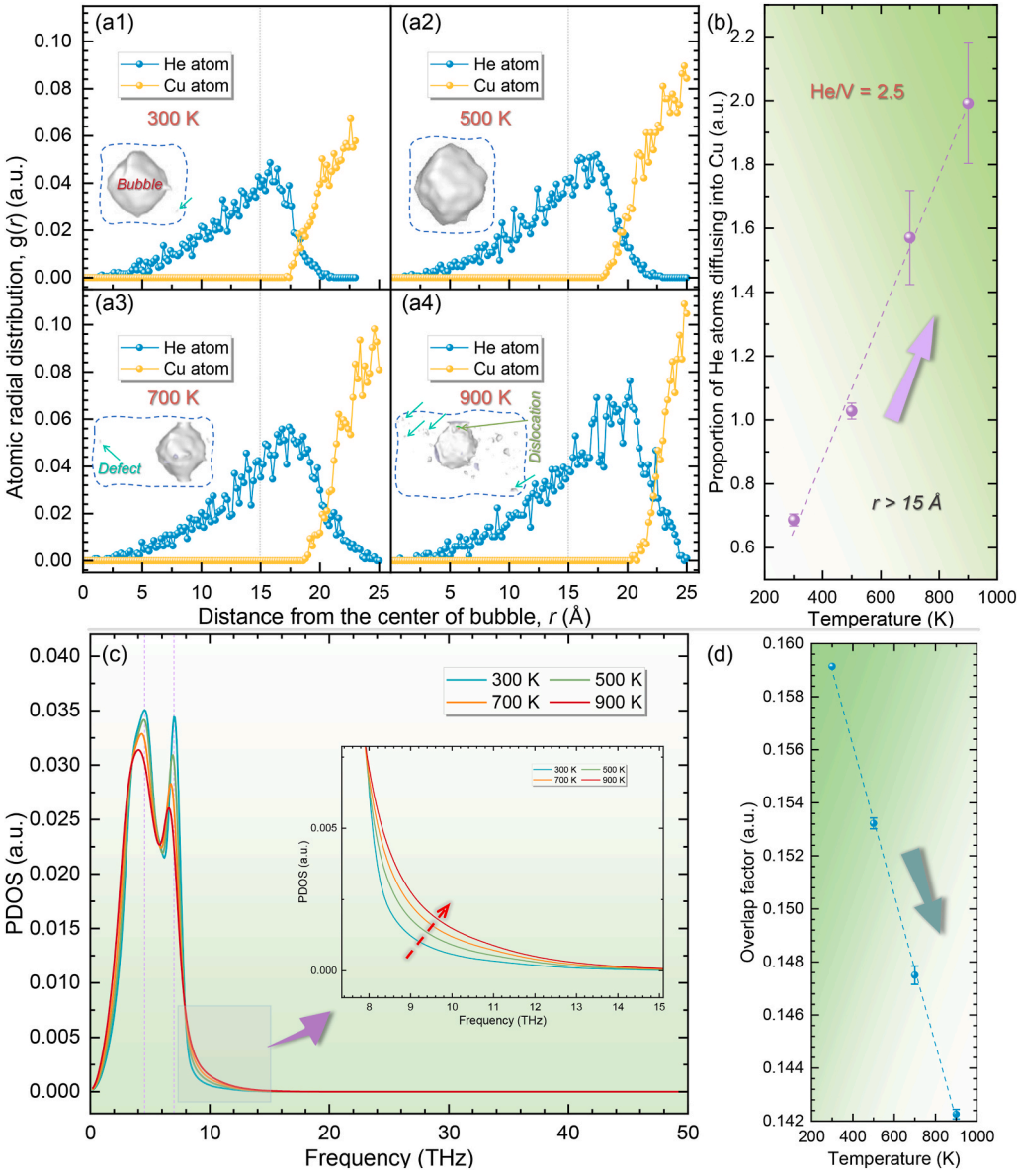

Fig. 10. Temperature-dependent microstructural and phononic evolution for the He/V = 2.5 system from 300 to 900 K. (**a**) Radial distribution functions of He and Cu atoms centered on the bubble; insets depict the corresponding defect structures near the interface. (**b**) Fraction of He atoms located beyond the original bubble radius (r > 15.0 Å) plotted against temperature. (**c**) PDOS spectra over the investigated temperature range. (**d**) PDOS overlap factor referenced to the spectrum at 300 K, plotted versus temperature to correlate spectral changes with the rise in interfacial thermal resistance.

confirming that the overpressurized bubble displaces lattice atoms as it grows. Concurrently, the deepening penetration of helium into the copper promotes clustering and the nucleation of dislocations and other defects [43,46,58], particularly at high temperatures (see inset of Fig. 10 (a4)). These microstructural changes—bubble enlargement and the generation of dispersed helium-related defects in the matrix—act synergistically to intensify phonon scattering, which accounts for the rapidly increasing Kapitza resistance observed in Fig. 9(b). The correlation is quantified in Fig. 10(b), which plots the fraction of He atoms located outside the original bubble radius ($r > 15.0$ Å) as a function of temperature. This fraction increases approximately linearly with temperature, reflecting the enhanced outward diffusion driven by elevated bubble pressure [43]. Its close correspondence with the trend in Kapitza resistance firmly establishes the positive relationship between helium diffusion and interfacial thermal resistance. Moreover, the deeper infusion of helium into the copper matrix at high temperatures (*e.g.*, 900 K, inset of Fig. 10(a4)) means that phonon scattering occurs not only at the bubble interface but also throughout the bulk material. This dual effect explains why the temperature profiles in Fig. 9(a) exhibit characteristics of both bubble-dominated systems (Fig. 4(a)) and systems containing dispersed interstitial helium (Fig. 2(a)): at elevated temperatures, thermal transport is hindered simultaneously by a strengthening interfacial barrier and by increased point-defect scattering within the copper lattice. To elucidate the temperature dependence of thermal transport in the helium-bubble system from a fundamental perspective, an analysis based on phonon dynamics was conducted. The temperature-dependent phonon spectrum and the corresponding PDOS overlap factor were calculated and are presented in Fig. 10(c) and (d), respectively. As shown in Fig. 10(c) and consistent with the interstitial-helium system, the PDOS peak intensities gradually weaken and the peaks broaden with rising temperature. This suppression and broadening reflect shortened phonon lifetimes and indicate a declining thermal transport capacity in the bubble-containing material. These spectral changes originate from the microstructural evolution induced by the bubble: the overpressurized bubble expands outward, displacing Cu atoms, while simultaneously facilitating the diffusion of helium into the surrounding lattice. The resulting lattice distortion, particularly near dislocations and defect clusters, strongly enhances phonon scattering. This effect becomes more pronounced at elevated temperatures, as the increased population of high-frequency phonons (see the highlighted region in the inset of Fig. 10(c)) provides more channels for inelastic and impurity-mediated scattering [78,79]. Complementing this picture, the PDOS overlap factor in Fig. 10(d) decreases approximately linearly with temperature, providing a quantitative measure of the progressive deviation of the vibrational spectrum from that of pristine copper. This linear decline aligns well with the dual influence of bubble expansion and the attendant alteration of phonon modes at high temperatures, reinforcing the conclusion that interfacial and defect-mediated scattering mechanisms are thermally activated and collectively govern the degradation of thermal transport in the system.

4. Conclusions

In summary, this study systematically elucidates the atomistic mechanisms of helium-induced thermal transport degradation in copper through NEMD simulations focused on three governing variables: interstitial helium concentration, helium bubble pressure (He/V ratio), and ambient temperature. For systems with dispersed helium, TC declines progressively, reaching a 47% reduction at 8000 appm. This degradation is directly correlated with the nucleation and growth of helium clusters, where the maximum cluster size increases from 6 to 12 atoms and the total cluster count rises linearly with concentration, intensifying phonon scattering and suppressing low-frequency modes as quantified by a decreasing PDOS overlap factor. In systems containing a nanoscale helium bubble, interfacial Kapitza resistance becomes the dominant barrier to heat flow, demonstrating a strong positive correlation with internal pressure—increasing by a factor of ~2.5, from 0.87 to 2.25 GW^{-1} m^2 K, as the He/V ratio rises from 0 to 3.0. A pivotal discovery is the anomalous positive temperature dependence of this interfacial resistance for the He/V = 2.5 system, which increases from 1.56 to 4.37 GW^{-1} m^2 K between 300 and 900 K, a trend contrary to conventional solid/solid interfaces and attributed to the unique compressible nature of the gas-filled bubble. Radial distribution analyses confirm that higher He/V ratios and temperatures promote outward helium diffusion and bubble growth, which simultaneously introduce lattice distortion and dislocation activity in the surrounding copper. Elevated temperatures universally exacerbate thermal transport degradation by activating two synergistic pathways: intensifying intrinsic phonon-phonon anharmonic scattering and thermally accelerating helium diffusion and clustering. This leads to a more rapid decline in TC, though the rate of decrease ($\sim 1/T^{0.838}$) is moderated relative to pristine copper due to a competing increase in the spectral weight of high-frequency phonons. This work therefore establishes a comprehensive microstructural framework in which helium impairs thermal transport through two primary and often concurrent mechanisms: point defect and cluster scattering within the matrix, and interface-dominated resistance from bubbles. This dual-mechanism framework offers a rational basis for guiding microstructural design strategies. For example, alloying elements that suppress helium clustering or modify bubble interface properties may help mitigate TC loss. Moreover, the observed anomalous positive temperature dependence of Kapitza resistance at bubble interfaces highlights the need for thermal management strategies to account for interface type (solid/gas *vs.* solid/solid) when predicting component performance under varying thermal loads. Future efforts should extend these atomistic insights to longer time scales using accelerated dynamics methods to capture slow helium migration and bubble evolution, and should explore the influence of alloying elements such as Cr and Zr on helium behavior and phonon scattering. Such studies will help bridge the gap between atomic-scale mechanisms and macroscopic component lifetime predictions, ultimately guiding the development of more radiation-tolerant heat sink materials for next-generation fusion devices.

CRediT authorship contribution statement

Rui Jin: Data curation, Formal analysis, Investigation, Methodology, Software, Visualization, Writing – original draft. **Hanlong Wang:** Data curation, Formal analysis, Investigation, Methodology, Software, Visualization. **Qing Peng:** Data curation, Formal analysis, Methodology, Validation. **Hai Huang:** Conceptualization, Funding acquisition, Project administration, Resources, Supervision, Writing – review & editing.

Declaration of competing interest

The authors declare that they have no known competing financial interests or personal relationships that could have appeared to influence the work reported in this paper.

Acknowledgements

This work was supported by the Natural Science Foundation of Henan (Grant No. 252300423007), the Young Talent Support Program of Henan Association for Science and Technology (Grant No. 2025HYTP047), the Key Project for Science and Technology Development of Henan Province (Grant No. 242102230052), the Training Program for Young Backbone Teachers in Zhengzhou University (Grant No. 2025ZDGGJS010), the Innovation Team Support Program for Cooperation of Young Talents & Enterprises in Zhengzhou University (Grant No. 35240767), and the National Supercomputing Center in Zhengzhou.

Data availability

Data will be made available on request.

References

[1] G. Katoch, G. Sharma, M. Alaghbari, A. Ved, J. Kaur, A. Rajiv, A. Singh, Y. Yadav, M.I. Khairandish, Fusion energy: a sustainable pathway to meeting future global energy demands, Discov. Sustain. 6 (2025) 221, https://doi.org/10.1007/s43621-025-00906-6.

[2] Y. Ueda, K. Schmid, M. Balden, J.W. Coenen, T. Loewenhoff, A. Ito, A. Hasegawa, C. Hardie, M. Porton, M. Gilbert, Baseline high heat flux and plasma facing materials for fusion, Nucl. Fusion 57 (2017) 092006, https://doi.org/10.1088/1741-4326/aa6b60.

[3] J. Linke, J. Du, T. Loewenhoff, G. Pintsuk, B. Spilker, I. Steudel, M. Wirtz, Challenges for plasma-facing components in nuclear fusion, Matter Radiat. Extremes 4 (2019) 056201, https://doi.org/10.1063/1.5090100.

[4] T. Liu, X. Ge, F. Chen, Y. Jiang, H. Huang, An experimental study on corrosion resistance of Ti35 alloy and its high-fluence hydrogen bombardment behavior, J. Phys. Chem. Solid. 201 (2025) 112646, https://doi.org/10.1016/j.jpcs.2025.112646.

[5] J. Knaster, P. Garin, H. Matsumoto, Y. Okumura, M. Sugimoto, F. Arbeiter, P. Cara, S. Chel, A. Facco, P. Favuzza, T. Furukawa, R. Heidinger, A. Ibarra, T. Kanemura, A. Kasugai, H. Kondo, V. Massaut, J. Molla, G. Micciche, S. O'hira, K. Sakamoto, T. Yokomine, E. Wakai, The IFMIF/EVEDA integrated project team, overview of the IFMIF/EVEDA projecta, Nucl. Fusion 57 (2017) 102016, https://doi.org/10.1088/1741-4326/aa6a6a.

[6] H. Xu, S.Y. Kim, D. Chen, J.P. Monchoux, T. Voisin, C. Sun, J. Li, Materials genomics search for possible helium-absorbing nano-phases in fusion structural materials, Adv. Sci. 9 (2022) 2203555, https://doi.org/10.1002/advs.202203555.

[7] X. Qian, X. Peng, Y. Song, X. Mao, P. Liu, W. Song, J. Huang, P. Lu, L. Wang, L. Meng, New designs of target and cooling scheme for water cooled divertor in DEMO, Nucl. Fusion 61 (2021) 036008, https://doi.org/10.1088/1741-4326/abd148.

[8] H. Huang, X. Tang, K. Xie, Q. Peng, Enhanced self-healing of irradiation defects near a Ni–graphene interface by damaged graphene: insights from atomistic modeling, J. Phys. Chem. Solid. 51 (2020) 109909, https://doi.org/10.1016/j.jpcs.2020.109909.

[9] S.J. Zinkle, Fusion materials science: overview of challenges and recent progress, Phys. Plasmas 12 (2005) 058101, https://doi.org/10.1063/1.1880013.

[10] L. Ma, T. Liu, B. Cai, Z. Liu, G. Zhang, J. Li, H. Li, H. Huang, Molecular dynamics studies of primary irradiation damage in α-type Ti35 alloy, Phys. Status Solidi B 260 (2023) 2200560, https://doi.org/10.1002/pssb.202200560.

[11] R.S. Averback, T.D. De La Rubia, Displacement damage in irradiated metals and semiconductors, Solid State Phys. 51 (1998) 281–402, https://doi.org/10.1016/S0081-1947(08)60193-9.

[12] B. Li, L. Wang, W. Jian, J. E, H. Ma, S. Luo, Irradiation-initiated plastic deformation in prestrained single-crystal copper, Nucl. Instrum. Methods B 368 (2016) 60–65, https://doi.org/10.1016/j.nimb.2015.12.011.

[13] Y.N. Osetsky, A. Serra, M. Victoria, S.I. Golubov, V. Priego, Vacancy loops and stacking-fault tetrahedra in copper: I. Structure and properties studied by pair and many-body potentials, Philos. Mag. 79 (1999) 2259–2283, https://doi.org/10.1080/01418619908210421.

[14] Y.N. Osetsky, D.J. Bacon, B.N. Singh, B. Wirth, Atomistic study of the generation, interaction, accumulation and annihilation of cascade-induced defect clusters, J. Nucl. Mater. 307 (2002) 852–861, https://doi.org/10.1016/S0022-3115(02)01094-2.

[15] F. Wu, Y. Zhu, Q. Wu, X. Li, P. Wang, H. Wu, Helium bubbles aggravated defects production in self-irradiated copper, J. Nucl. Mater. 496 (2017) 265–273, https://doi.org/10.1016/j.jnucmat.2017.09.042.

[16] X. Yu, T. Wang, T. Hu, H. Huang, Preexisting helium effects on primary radiation damage in copper: atomic-scale insights from molecular dynamics simulations, Eur. Phys. J. Plus. 141 (2026) 41, https://doi.org/10.1140/epjp/s13360-025-07268-y.

[17] H. Trinkaus, Possible mechanisms limiting the pressure in inert gas bubbles in metals, in: S.E. Donnelly, J.H. Evans (Eds.), Fundamental Aspects of Inert Gases in Solids, Springer, Boston, 1991, pp. 369–383.

[18] B. Li, L. Wang, J. E, H. Ma, S.N. Luo, Shock response of He bubbles in single crystal Cu, J. Appl. Phys. 116 (2014) 213506, https://doi.org/10.1063/1.4903732.

[19] W. Qin, W. Guo, T. Cheng, J. Tang, C. Jiang, F. Ren, Review on helium behaviors in nanochannel tungsten film, Tungsten 3 (2021) 369–381, https://doi.org/10.1007/s42864-021-00097-3.

[20] T. Yamamoto, G.R. Odette, P. Miao, D.J. Edwards, R.J. Kurtz, Helium effects on microstructural evolution in tempered martensitic steels: in situ helium implanter studies in HFIR, J. Nucl. Mater. 386 (2009) 338–341, https://doi.org/10.1016/j.jnucmat.2008.12.134.

[21] C. Cawthorne, E.J. Fulton, Voids in irradiated stainless steel, Nature 216 (1967) 575–576, https://doi.org/10.1038/216575a0.

[22] P.D. Edmondson, C.M. Parish, Y. Zhang, A. Hallén, M.K. Miller, Helium bubble distributions in a nanostructured ferritic alloy, J. Nucl. Mater. 434 (2013) 210–216, https://doi.org/10.1016/j.jnucmat.2012.11.049.

[23] S.J. Zinkle, L.L. Snead, Designing radiation resistance in materials for fusion energy, Annu. Rev. Mater. Res. 44 (2014) 241–267, https://doi.org/10.1146/annurev-matsci-070813-113627.

[24] G. Kalinin, R. Matera, Comparative analysis of copper alloys for the heat sink of plasma facing components in ITER, J. Nucl. Mater. 258 (1998) 345–350, https://doi.org/10.1016/S0022-3115(98)00271-2.

[25] G. Kalinin, V. Barabash, A. Cardella, J. Dietz, K. Ioki, R. Matera, R.T. Santoro, R. Tivey, Assessment and selection of materials for ITER in-vessel components, J. Nucl. Mater. 283 (2000) 10–19, https://doi.org/10.1016/S0022-3115(00)00305-6.

[26] S.A. Fabritsiev, S.J. Zinkle, B.N. Singh, Evaluation of copper alloys for fusion reactor divertor and first wall components, J. Nucl. Mater. 233 (1996) 127–137, https://doi.org/10.1016/S0022-3115(96)00091-8.

[27] G. Federici, W. Biel, M.R. Gilbert, R. Kemp, N. Taylor, R. Wenninger, European DEMO design strategy and consequences for materials, Nucl. Fusion 57 (2017) 092002, https://doi.org/10.1088/1741-4326/57/9/092002.

[28] S.A. Fabritsiev, A.S. Pokrovskii, V.R. Barabash, Y.G. Prokofiev, Neutron spectrum and transmutation effects on the radiation damage of copper alloys, Fusion Eng. Des. 36 (1997) 505–513, https://doi.org/10.1016/S0920-3796(96)00700-4.

[29] D. Terentyev, M. Rieth, G. Pintsuk, A. Von Müller, S. Antusch, A. Zinovev, A. Bakaev, K. Poleshchuk, G. Aiello, Effect of neutron irradiation on tensile properties of advanced Cu-based alloys and composites developed for fusion applications, J. Nucl. Mater. 584 (2023) 154587, https://doi.org/10.1016/j.jnucmat.2023.154587.

[30] T. Yamamoto, Y. Wu, K. Yabuuchi, J. Haley, K. Yoshida, A. Kimura, G.R. Odette, Cavity evolution and void swelling in dual ion irradiated tempered martensitic steels, J. Nucl. Mater. 576 (2023) 154201, https://doi.org/10.1016/j.jnucmat.2022.154201.

[31] X. Ye, Z. He, B. Pan, The thermal conductivity of defected copper at finite temperatures, J. Mater. Sci. 55 (2020) 4453–4463, https://doi.org/10.1007/s10853-019-04267-0.

[32] E. Trachanas, A. Wylie, A. Bignami, N. Gazis, M.P. Short, K. Michel, C. Alwmark, E. Gazis, G. Fikioris, H. Danared, Study of thermal diffusivity degradation on Cu-OFE copper due to proton and self-ion irradiation using in situ transient grating spectroscopy, J. Nucl. Mater. 607 (2025) 155674, https://doi.org/10.1016/j.jnucmat.2025.155674.

[33] W. Sun, S. Gu, B. Ji, Q. Qi, H. Zhou, G. Luo, Effects of he irradiation on the microstructure and thermal conductivity of SiC, Nucl. Fusion 65 (2025) 096017, https://doi.org/10.1088/1741-4326/adf75d.

[34] S.A. Fabritsiev, A.S. Pokrovsky, Effect of high doses of neutron irradiation on physico-mechanical properties of copper alloys for ITER applications, Fusion Eng. Des. 73 (2005) 19–34, https://doi.org/10.1016/j.fusengdes.2004.12.003.

[35] H. Huang, X. Ge, X. Yu, Y. Jiang, Q. Peng, Atomistic studies of helium trapping and diffusion at Ni−graphene interfaces, Eur. Phys. J. Plus. 140 (2025) 497, https://doi.org/10.1140/epjp/s13360-025-06447-1.

[36] K. Nordlund, S.J. Zinkle, A.E. Sand, F. Granberg, R.S. Averback, R.E. Stoller, T. Suzudo, L. Malerba, F. Banhart, W.J. Weber, F. Willaime, S.L. Dudarev, D. Simeone, Primary radiation damage: a review of current understanding and models, J. Nucl. Mater. 512 (2018) 450–479, https://doi.org/10.1016/j.jnucmat.2018.10.027.

[37] M. Boleininger, D.R. Mason, T. Schwarz-Selinger, P. Ma, Atomistic simulations of irradiation damage on the engineering timescale: examining the dose rate effect in tungsten, Mater. Adv. 6 (2025) 7379–7394, https://doi.org/10.1039/D5MA00677E.

[38] Q. Wang, N. Gui, X. Huang, X. Yang, J. Tu, S. Jiang, The effect of temperature and Cascade collision on thermal conductivity of 3C-SiC: a molecular dynamics study, Int. J. Heat Mass Tran. 180 (2021) 121822, https://doi.org/10.1016/j.ijheatmasstransfer.2021.121822.

[39] H. Zhang, Y. Wang, J. Sun, M. Qin, T. Stirner, Lattice thermal conductivity of defected tungsten evaluated by equilibrium molecular dynamics simulation, Mater. Today Commun. 36 (2023) 106495, https://doi.org/10.1016/j.mtcomm.2023.106495.

[40] C.L.M. Petersson, A. Fredriksson, S. Melin, A. Ahadi, P. Hansson, A molecular dynamics study on the influence of vacancies and interstitial helium on mechanical properties of tungsten, J. Nucl. Mater. 580 (2023) 154378, https://doi.org/10.1016/j.jnucmat.2023.154378.

[41] S.S. Sharma, A. Parashar, Effect of helium on thermal transport properties in Single- and Bi-Crystals of ni: a study based on molecular dynamics, J. Phys. Appl. Phys. 57 (2024) 055304, https://doi.org/10.1088/1361-6463/ad056b.

[42] A. Kashinath, M.J. Demkowicz, A predictive interatomic potential for He in Cu and Nb, Model. Simul. Mater. Sc. 19 (2011) 035007, https://doi.org/10.1088/0965-0393/19/3/035007.

[43] L. Hu, B.D. Wirth, D. Maroudas, Thermal conductivity of tungsten: effects of plasma-related structural defects from molecular-dynamics simulations, Appl. Phys. Lett. 111 (2017) 081902, https://doi.org/10.1063/1.4986956.

[44] H. Zhang, J. Sun, Y. Wang, T. Stirner, A.Y. Hamid, C. Sang, Study of lattice thermal conductivity of tungsten containing bubbles by molecular dynamics simulation, Fusion Eng. Des. 161 (2020) 112004, https://doi.org/10.1016/j.fusengdes.2020.112004.

[45] Y. Ding, X. Wu, J. Zhan, Z. Chen, S. Mao, M. Ye, Simulation study of effects of grain boundary and helium bubble on lattice thermal resistance of tungsten, Fusion Eng. Des. 168 (2021) 112682, https://doi.org/10.1016/j.fusengdes.2021.112682.

[46] X. Yu, H. Wang, H. Huang, Investigating helium-induced thermal conductivity degradation in fusion-relevant copper: a molecular dynamics approach, Materials 18 (2025) 3702, https://doi.org/10.3390/ma18153702.

[47] H.S. Lima, C. Tsallis, Ising chain: thermal conductivity and first-principle validation of Fourier's law, Phys. Stat. Mech. Its Appl. 628 (2023) 129161, https://doi.org/10.1016/j.physa.2023.129161.

[48] S. Sæther, M.F. Erichsen, S. Xiao, Z. Zhang, A. Lervik, J. He, Phonon thermal transport in copper: the effect of size, crystal orientation, and grain boundaries, AIP Adv. 12 (2022) 065301, https://doi.org/10.1063/5.0094170.
[49] S. Plimpton, Fast parallel algorithms for short-range molecular dynamics, J. Comput. Phys. 117 (1995) 1–19, https://doi.org/10.1006/jcph.1995.1039.
[50] A. Stukowski, Visualization and analysis of atomistic simulation data with OVITO–the open visualization tool, Model. Simulat. Mater. Sci. Eng. 18 (2009) 015012, https://doi.org/10.1088/0965-0393/18/1/015012.
[51] T. Liang, M. Zhou, P. Zhang, P. Yuan, D. Yang, Multilayer In-Plane graphene/hexagonal boron nitride heterostructures: insights into the interfacial thermal transport properties, Int. J. Heat Mass Tran. 151 (2020) 119395, https://doi.org/10.1016/j.ijheatmasstransfer.2020.119395.
[52] MdH. Rahman, E.H. Chowdhury, M.R. Bin Shahadat, M.M. Islam, Engineered defects to modulate the phonon thermal conductivity of silicene: a nonequilibrium molecular dynamics study, Comput. Mater. Sci. 191 (2021) 110338, https://doi.org/10.1016/j.commatsci.2021.110338.
[53] L. Li, L. Peng, J. Shi, W. Jiang, Large helium-vacancy clusters coalescence during helium bubble evolution under Cascade in iron with edge dislocation: a MD simulation, Comput. Mater. Sci. 197 (2021) 110601, https://doi.org/10.1016/j.commatsci.2021.110601.
[54] MdS. Islam, I. Mia, A.S.M.J. Islam, C. Stampfl, J. Park, Temperature and interlayer coupling induced thermal transport across graphene/2D-SiC van der Waals heterostructure, Sci. Rep. 12 (2022) 761, https://doi.org/10.1038/s41598-021-04740-4.
[55] H. Huang, Y. Zhong, B. Cai, J. Wang, Z. Liu, Q. Peng, Size-and temperature-dependent thermal transport across a Cu−diamond interface: non-equilibrium molecular dynamics simulations, Surf. Interfaces 37 (2023) 102736, https://doi.org/10.1016/j.surfin.2023.102736.
[56] Z. Lu, A.M. Chaka, P.V. Sushko, Thermal conductance enhanced via inelastic phonon transport by atomic vacancies at Cu/Si interfaces, Phys. Rev. B 102 (2020) 075449, https://doi.org/10.1103/PhysRevB.102.075449.
[57] M.N. Luckyanova, J. Mendoza, H. Lu, B. Song, S. Huang, J. Zhou, M. Li, Y. Dong, H. Zhou, J. Garlow, L. Wu, B.J. Kirby, A.J. Grutter, A.A. Puretzky, Y. Zhu, M. S. Dresselhaus, A. Gossard, G. Chen, Phonon localization in heat conduction, Sci. Adv. 4 (2018), https://doi.org/10.1126/sciadv.aat9460.
[58] A.K. Shargh, O. Bosić, N. Abdolrahim, Mechanisms of helium nanobubble growth and defect interactions in irradiated copper: a molecular dynamics study, J. Nucl. Mater. 574 (2023) 154199, https://doi.org/10.1016/j.jnucmat.2022.154199.
[59] V. Karthikeyan, C.M. Arava, M.Z. Hlaing, B. Chen, C.H. Chan, K.H. Lam, V.A. L. Roy, Dislocation-induced ultra-low lattice thermal conductivity in rare Earth doped β-Zn4Sb3, Scr. Mater. 174 (2020) 95–101, https://doi.org/10.1016/j.scriptamat.2019.08.037.
[60] Y. Cheng, M. Nomura, S. Volz, S. Xiong, Phonon–dislocation interaction and its impact on thermal conductivity, J. Appl. Phys. 130 (2021) 040902, https://doi.org/10.1063/5.0054078.
[61] R. Zheng, W. Jian, I.J. Beyerlein, W. Han, Atomic-scale hidden point-defect complexes induce ultrahigh-irradiation hardening in tungsten, Nano Lett. 21 (2021) 5798–5804, https://doi.org/10.1021/acs.nanolett.1c01637.
[62] A. Neogi, H. Askari, N. Abdolrahim, Elastic and plastic deformation behavior of helium nano-bubbled single crystal copper: an atomistic simulation study, J. Nucl. Mater. 552 (2021) 152988, https://doi.org/10.1016/j.jnucmat.2021.152988.
[63] J. Li, I.J. Beyerlein, W. Han, Helium irradiation-induced ultrahigh hardening in niobium, Acta Mater. 226 (2022) 11765, https://doi.org/10.1016/j.actamat.2022.117656.
[64] C. Zhang, H. Zhou, Y. Zeng, L. Zheng, Y. Zhan, K. Bi, A reduction of thermal conductivity of non-periodic Si/Ge superlattice nanowire: molecular dynamics simulation, Int. J. Heat Mass Tran. 132 (2019) 681–688, https://doi.org/10.1016/j.ijheatmasstransfer.2018.12.041.
[65] L. Momenzadeh, A.V. Evteev, E.V. Levchenko, I.V. Belova, G.E. Murch, Y.H. Sohn, Phonon thermal conductivity of F.C.C. Cu by molecular dynamics simulation, Defect Diffusion Forum 336 (2013) 169–184. https://dx.doi.org/10.4028/www.scientific.net/DDF.336.169.
[66] G. Qin, Z. Qin, H. Wang, M. Hu, Anomalously temperature-dependent thermal conductivity of monolayer GaN with large deviations from the traditional 1/T law, Phys. Rev. B 95 (2017) 195416, https://doi.org/10.1103/PhysRevB.95.195416.
[67] J. Fang, H. Deng, W. Hu, N. Gao, Y. Tong, Y. Hu, S. Wang, K. Wang, Influence of temperature gradients on helium diffusion and clustering in tungsten: a molecular dynamics study, Fusion Eng. Des. 208 (2024) 114687, https://doi.org/10.1016/j.fusengdes.2024.114687.
[68] R. Chen, A.I. Hochbaum, P. Murphy, J. Moore, P. Yang, A. Majumdar, Thermal conductance of thin silicon nanowires, Phys. Rev. Lett. 101 (2008) 105501, https://doi.org/10.1103/PhysRevLett.101.105501.
[69] M. Hu, D. Poulikakos, Si/Ge superlattice nanowires with ultralow thermal conductivity, Nano Lett. 12 (2012) 5487–5494, https://doi.org/10.1021/nl301971k.
[70] D. Li, Y. Wu, P. Kim, L. Shi, P. Yang, A. Majumdar, Termal conductivity of individual silicon nanowires, Appl. Phys. Lett. 83 (2003) 2934, https://doi.org/10.1063/1.1616981.
[71] G. Xie, D. Ding, G. Zhang, Phonon coherence and its effect on thermal conductivity of nanostructures, Adv. Phys. X 3 (2018) 1480417, https://doi.org/10.1080/23746149.2018.1480417.
[72] P. Pichanusakorn, P. Bandaru, Nanostructured thermoelectrics, Mater. Sci. Eng. R 67 (2010) 19–63, https://doi.org/10.1016/j.mser.2009.10.001.
[73] S. Xiong, Y.A. Kosevich, K. Sääskilahti, Y. Ni, S. Volz, Tunable thermal conductivity in silicon twinning superlattice nanowires, Phys. Rev. B 90 (2014) 195439, https://doi.org/10.1103/PhysRevB.90.195439.
[74] S. Xiong, D. Selli, S. Neogi, D. Donadio, Native surface oxide turns alloyed silicon membranes into nanophononic metamaterials with ultralow thermal conductivity, Phys. Rev. B 95 (2017) 180301, https://doi.org/10.1103/PhysRevB.95.180301.
[75] L. Van Brutzel, A. Chartier, A new equation of state for helium nanobubbles embedded in UO2 matrix calculated via molecular dynamics simulations, J. Nucl. Mater. 518 (2019) 431–439, https://doi.org/10.1016/j.jnucmat.2019.02.015.
[76] W. Wu, J. Shao, Y. Qie, Atomistic insight into the thermodynamic properties and the surrounding deformation of high-pressurized he bubbles in Al, Comput. Mater. Sci. 180 (2020) 109699, https://doi.org/10.1016/j.commatsci.2020.109699.
[77] E.S. Landry, A.J.H. McGaughey, Thermal boundary resistance predictions from molecular dynamics simulations and theoretical calculations, Phys. Rev. B 80 (2009) 165304, https://doi.org/10.1103/PhysRevB.80.165304.
[78] S. Kim, D.T. Ho, K. Kang, S.Y. Kim, Phonon scattering during dislocation motion inducing stress-drop in cubic metals, Acta Mater. 115 (2016) 143–154, https://doi.org/10.1016/j.actamat.2016.05.053.
[79] S. Xu, X. Chen, Modeling dislocations and heat conduction in crystalline materials: atomistic/continuum coupling approaches, Int. Mater. Rev. 64 (2019) 407–438, https://doi.org/10.1080/09506608.2018.1486358.